IEEE Access
Multidisciplinary | Rapid Review | Open Access Journal

Received January 31, 2022, accepted February 19, 2022, date of publication February 24, 2022, date of current version March 4, 2022.

Digital Object Identifier 10.1109/ACCESS.2022.3154481

Stator Current Spectral Content of Inverter-Fed Cage Rotor Induction Motor

GOJKO JOKSIMOVIĆ[1], (Senior Member, IEEE), PETER ZAJEC[2], (Member, IEEE), ALBERTO TESSAROLO[3], (Senior Member, IEEE), VANJA AMBROŽIČ[2], (Senior Member, IEEE), AND ANDRAŽ RIHAR[2], (Member, IEEE)

[1]Faculty of Electrical Engineering, University of Montenegro, 81000 Podgorica, Montenegro
[2]Faculty of Electrical Engineering, University of Ljubljana, 1000 Ljubljana, Slovenia
[3]Department of Engineering and Architecture, University of Trieste, 34127 Trieste, Italy

Corresponding author: Gojko Joksimović (gojko.joksimovic@ucg.ac.me)

This work was supported in part by the Ministry of Science of Montenegro under Grant Induction Motor Efficiency Improvement Through Optimal Electromagnetic Design Solutions—Induction Motor Efficiency Improvement (IMEI); and in part by the Ministry of Science of Montenegro and Slovenian Research Agency, Slovenia, (Poboljšanje energetske efikasnosti invertorski napajanog asinhronog motora adekvatnim izborom broja štapova rotora) under Bilateral Grant BI-ME/18-20-016.

ABSTRACT The paper analyzes the influence of the number of rotor bars on the stator current spectral content in a three-phase cage induction motor fed by a pulse-width modulated (PWM) inverter. It is shown that each of the higher-order time harmonics in the supply voltage produces space harmonics in a rotating magnetic flux density wave, which results in induced rotor slot harmonics (RSHs) in the stator current spectrum. The conditions for the existence of these space harmonics are identical to those applying to a mains-fed motor. In other words, the number of rotor bars of a mains-fed motor yielding an RSH-free stator current spectrum produces the same stator current spectrum even in case the motor is inverter-fed. Additionally, to minimize the adverse effects of RSHs in the stator current spectrum, one must consider not only the number of rotor bars, but also its relationship with the frequency modulation ratio of the PWM inverter. Analytical predictions are presented to illustrate these results supported both by numerical simulations of the induction motor modelled through the winding function theory and experimentally taking the case a two-pole cage induction machine as a case study.

INDEX TERMS Amplitude modulation, frequency modulation, induction motors, pulse width modulation, power converter harmonics.

I. INTRODUCTION

After more than a century since their invention, induction motors still play a paramount importance in industry and vehicle traction applications over a huge variety of ratings, thanks to their cheapness, ruggedness and reliability [1]–[3]. The ongoing need to limit the use rare earths due to fluctuating cost, environmental and availability issues is promoting a renewed interest in the exploitation of induction motors [4] as preferred alternative to permanent-magnet machines whenever possible. For sure, more and more efforts are being placed on the attempt to improve the performance of induction motors under various respects, such as increasing their efficiency to meet present energy saving standards and targets [5] as well as reducing noise and vibrations [6]. These targets apply to traditional mains-fed motor but are even more relevant to inverter-fed motors, which account for the vast majority today thanks to their capability of operating at variable speed. Several approaches can be pursued to improve the performance of inverter-fed induction motors. Recently interesting approaches have been proposed based on advanced and smartly designed supply, automation and management techniques where the main focus is on the inverter technology and control [2], [3], [5], [6]. In contrast, an apparent lack appears in the literature regarding the potentials of acting on the induction motor design to optimize its operation when supplied from a PWM inverter.

Recent research, conducted on mains-fed induction motors, has highlighted the importance of an appropriate selection of the number of rotor bars, for example, to minimize Rotor Slot Harmonics (RSHs) and their relevant parasitic effect under sinusoidal supply [7], [8]. The main goal

The associate editor coordinating the review of this manuscript and approving it for publication was Qinfen Lu.

of the paper is to extend the discussion and results presented in [7] and [8] covering the case of inverter-fed motors. The main problem being considered is how some key design choices such as the selection of the number of stator slots and rotor bars, for a given number of poles, can affect the performance of the induction motor when it is fed from a PWM inverter. To this end, a preliminary analysis will be firstly presented of the supply voltage spectrum from an inverter-fed induction motor in order to identify a simple but comprehensive model for the time harmonics produced at the inverter output. As a further step, the air-gap magnetic fields caused by PWM-related time harmonics will be identified along with the generation mechanism of RSHs. Conditions will be then derived for the occurrence of RSHs of different possible orders in the stator current spectrum. This will finally lead to identify some practical rules to avoid and minimize RSHs, with special regard to low-frequency low-order ones, which can have the worst impact on motor performance. It will be shown how in case of inverter-fed motors, the selection of the number of stator and rotor slots, for any given number of pole pairs, is not the only useful criterion to follow, as an essential role is played by the PWM modulation ratio. It will be thus shown how the inverter-fed induction motor needs to be optimized not as a stand-alone component, but together with the particular inverter which supplies it and depending on the particular PWM modulation ratio to be used.

The main results presented will be illustrated through numerical simulations and through measurements on a dedicated experimental setup.

II. ANALYSIS OF THE VOLTAGE SPECTRAL CONTENT AT THE PWM-INVERTER OUTPUT

Here, a detailed analysis of the voltage spectral content at the output of a carrier-based PWM with min-max sequence injection is performed. It is worth mentioning that bipolar PWM with min-max sequence injection produces the same pulse pattern as that of the space vector modulation (SVM), with the center-weighted seven-segment vector sequence [9]. However, considering the easy implementation of carrier-based PWM, and the availability of PWM outputs in most digital platforms, the slight modification of the reference signal using min-max is a straightforward way of achieving to center-weighted SVM equivalent operation without complex algorithms, calculations, and vector generation sequence. For that reason, carrier-based PWM with min-max can be considered for spectrum derivation. As a result of this analysis, approximate analytical expressions that describe the line-to-line voltage at the input of the three-phase induction motor are illustrated.

As it is well known, the use of PWM inverters allows the simultaneous change of the motor supply voltage both in terms of the rms value and frequency. In this paper, a PWM frequency converter in synchronous mode is analyzed, i.e., in the case where the frequency modulation ratio m_f between the carrier frequency f_c and the modulation frequency f_m,

$$m_f = f_c/f_m, \tag{1}$$

is an integer [10], [11]. The carrier frequency is the frequency of the triangular wave, while the modulation frequency is that of the desired voltage fundamental at the inverter output. To eliminate the even harmonics at low values of m_f, an odd integer number is preferred for m_f [10]. In this particular case, the spectral content of the voltage signal at the PWM inverter output will be analyzed for $m_f = 15$. This case corresponds to a triangular wave signal with a carrier frequency $f_c = 750$ Hz and a modified sinusoidal signal with a modulation frequency $f_m = 50$ Hz.

Another critical parameter in PWM is the modulation index m_a, which is the ratio between the amplitude of the modulation wave A_m and the amplitude of the carrier wave A_c:

$$m_a = A_m/A_c. \tag{2}$$

By analyzing the output phase voltage waveform, obtained by comparison of carrier and modulating wave through min-max sequence injection, Fig. 1, it can be easily shown that, apart from the fundamental frequency wave, phase voltage contains a dc component, together with higher-order time harmonics of the following orders: m_f, $m_f \pm 2$, $m_f \pm 4$, $2m_f \pm 1$, $2m_f \pm 3$, $2m_f \pm 5$, $3m_f$, $3m_f \pm 2$, $3m_f \pm 4$, etc. The order of these harmonics is generally described by the following expressions [10], [11],

$$f_h = h \cdot f_1, \tag{3}$$

$$h = j \cdot m_f \pm k, \tag{4}$$

where for odd values of j the harmonics exist only for even values of k. For even values of j, the harmonics exist only for odd values of k. In contrast, for a frequency modulation ratio $m_f \geq 9$, the harmonic amplitudes are almost independent of m_f, though m_f defines their occurrence frequencies [10].

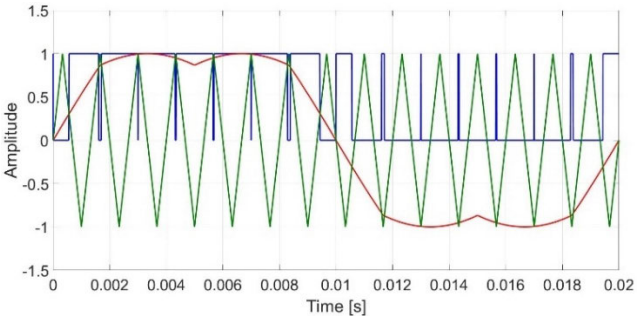

FIGURE 1. Crossing points of carrier and modulating wave define the PWM phase voltage: $f_c = 750$ Hz, $f_m = 50$ Hz, $m_f = 15$, $m_a = 1.1547$, $U_{dc} = 1$ V.

In addition, some of the harmonics i.e. of m_f, $2m_f \pm 3$, $3m_f$ orders are absent in the line-to-line voltages, as the phase voltages in all three phases are in-phase, thus cancelling their impact as it is depicted in Fig. 2 and Fig. 3, for two different modulation indexes.

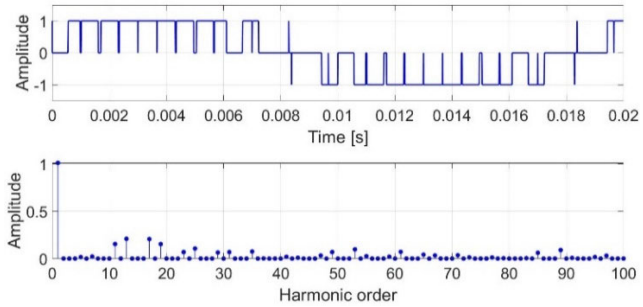

FIGURE 2. Line-to-line voltage and its spectral content: $f_c = 750$ Hz, $f_m = 50$Hz, $m_f = 15$, $m_a = 1.1547$, $U_{dc} = 1$ V.

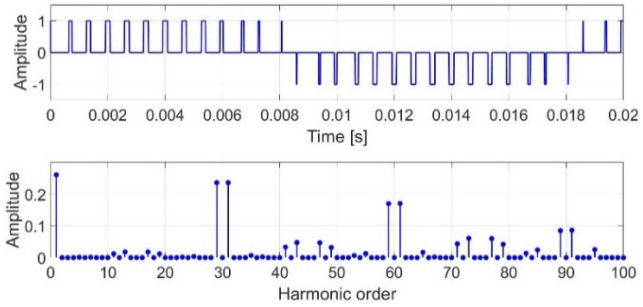

FIGURE 3. Line-to-line voltage and its spectral content: $f_c = 750$ Hz, $f_m = 50$Hz, $m_f = 15$, $m_a = 0.3$, $U_{dc} = 1$ V.

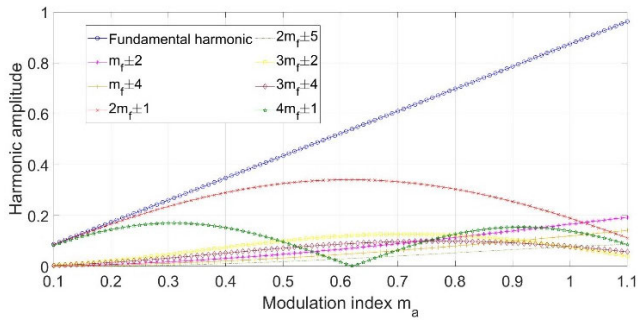

FIGURE 4. Amplitudes of the fundamental harmonic and first seven pairs of higher-order time harmonics in the line-to-line voltages versus modulation index m_a: $f_c = 750$ Hz, $f_m = 50$ Hz, $m_f = 15$, $U_{dc} = 1$ V.

Accordingly, in the line-to-line voltages at the output of the converter, apart from the fundamental, higher-order time harmonics also appear, the most prominent ones having orders $2m_f \pm 1$, $4m_f \pm 1$, $3m_f \pm 2$, $3m_f \pm 4$, $m_f \pm 2$. Which group would be particularly prominent depends on the value of the modulation index m_a, Fig. 4.

Furthermore, harmonic analysis shows that time harmonics of orders $m_f - 2$, $2m_f + 1$, $3m_f - 2$, $3m_f + 4$, $4m_f + 1$ form a positive sequence of voltages, while those of the orders $m_f + 2$, $2m_f - 1$, $3m_f + 2$, $3m_f - 4$, $4m_f - 1$ form an inverse, i.e., negative sequence of line-to-line three-phase voltages. It is also interesting to note that the harmonics from the same group have identical amplitudes.

As shown in Fig. 4, the fundamental increases linearly with the modulation index as long as the value of the modulation index is less than 1.1547 [9]. In the following, only the influence of harmonics from the first five groups will be considered, namely harmonics of orders $m_f \pm 2$, $2m_f \pm 1$, $3m_f \pm 2$, $3m_f \pm 4$ and $4m_f \pm 1$, respectively. Their normalized amplitudes can be analytically interpolated:

$$U_m = 0.876 \cdot m_a - 0.0022, \tag{5}$$

$$U_{m1} = 0.12 \cdot m_a^2 + 0.054 \cdot m_a - 0.0079, \tag{6}$$

$$U_{m2} = -0.983 \cdot m_a^2 + 1.209 \cdot m_a - 0.0345, \tag{7}$$

$$U_{m3} = 0.624 \cdot m_a^4 - 1.8962 \cdot m_a^3 + 1.5274 \cdot m_a^2 - 0.1926 \cdot m_a + 0.0135 \tag{8}$$

$$U_{m4} = 0.3063 \cdot m_a^4 - 1.039 \cdot m_a^3 + 0.9054 \cdot m_a^2 - 0.1013 \cdot m_a + 0.0071 \tag{9}$$

$$U_{m5} = \begin{cases} -1.8428 \cdot m_a^2 + 1.1451 \cdot m_a - 0.0109 \\ \qquad \text{for } 0.1 \le m_a < 0.62 \\ -1.8442 \cdot m_a^2 + 3.3716 \cdot m_a - 1.3891 \\ \qquad \text{for } 0.62 \le m_a < 1.15 \end{cases} \tag{10}$$

where U_{mn} indicates the amplitude of the n-th group of harmonics. In a real three-phase bridge inverter, all of the above amplitudes, (5)-(10), should be multiplied by U_{dc} equal to $(3\sqrt{2}/\pi)U_{LL}$.

The harmonic analysis leads to the following conclusion: the phase shift of harmonic voltages in relation to the fundamental is independent of the modulation index m_a, except for the fifth set of higher-order harmonics, where it shifts by $\pm\pi$ when the modulation index is higher than $m_a = 0.62$. However, this coincides in all three phases, so the voltage sequence remains the same – positive sequence for $4m_f + 1$ and negative for $4m_f - 1$.

Therefore, the input line-to-line voltage U_{ab} of a motor fed by a PWM inverter can be modeled by (11) and (12), as shown at the bottom of the next page, where $\alpha = \pi/3$. The amplitudes of the voltage components depend on the modulation index m_a, according to (5)-(10).

Similar expressions for the other two line-to-line voltages can be derived from previous conclusions considering a specific harmonic component positive or negative voltage sequence. if $m_a < 0.62$, otherwise:

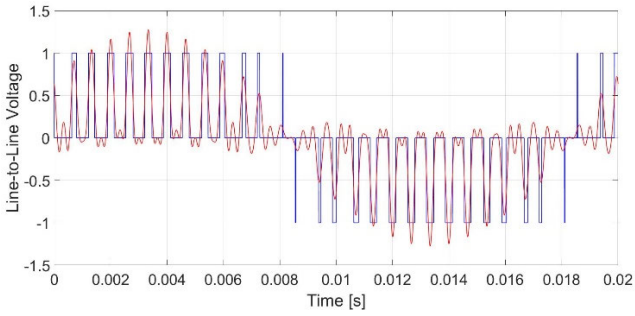

FIGURE 5. Line-to-line voltage U_{ab} at the output of PWM inverter (blue line) and its approximation (red line) obtained through derived analytical expressions: $m_a = 0.45$, $f_c = 750$ Hz, $f_m = 50$ Hz, $m_f = 15$, $U_{dc} = 1$ V.

Fig. 5 and Fig. 6 illustrate the application of the derived expressions for two different modulation index values.

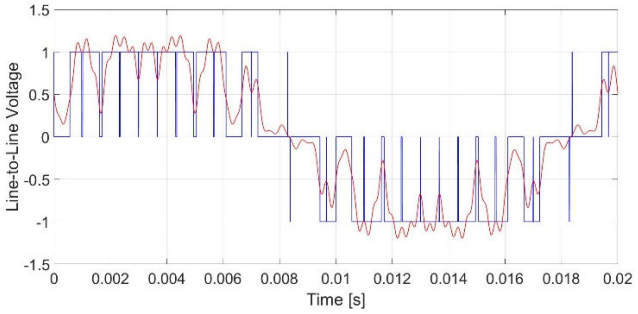

FIGURE 6. Line-to-line voltage U_{ab} at the output of PWM inverter (blue line) and its approximation (red line) obtained through derived analytical expressions: $m_a = 1.1547$, $f_c = 750$ Hz, $f_m = 50$ Hz, $m_f = 15$, $U_{dc} = 1$ V.

III. ROTOR SLOT HARMONICS IN THE STATOR CURRENT SPECTRUM–MAINS-FED MOTOR

In the case of a symmetrical three-phase cage induction motor, fed by a symmetrical three-phase AC voltage, the existence of rotor slot harmonics (RSHs) of order λ in the stator current spectrum is directly related to the number of rotor bars R and the number of pole pairs p [7], [8]. For $\lambda = 1$, we have rotor slot harmonics of the first order, the so-called principal slot harmonics, PSHs.

The condition for the existence of the lower RSH of order λ in the stator current spectrum, at the frequency

$$f^{\lambda}_{lower} = \left(1 - \lambda \frac{R}{p}(1-s)\right) \cdot f_1, \tag{13}$$

where f_1 indicates the mains frequency and s the slip, is given by the following relationship between the number of rotor bars and the number of pole pairs,

$$R^{\lambda}_{lower} = \frac{2p\,(3z+1)}{\lambda}, \tag{14}$$

where z is a theoretically arbitrary integer. In real situations, the number of rotor bars is usually in the range of $0.5S \leq R \leq 1.5S$, where S is the number of stator slots. Hence, the range of the integer z is $1 \leq z \leq 3\lambda S/(4mp)$ where m is number of phases.

The condition for the existence of the upper RSH of order λ in the stator current spectrum, at the frequency

$$f^{\lambda}_{upper} = \left(1 + \lambda \frac{R}{p}(1-s)\right) \cdot f_1, \tag{15}$$

is the following relationship between the number of rotor bars and the number of pole pairs:

$$R^{\lambda}_{upper} = \frac{2p\,(3z-1)}{\lambda} \tag{16}$$

In particular, if the number of rotor bars is

$$R^{\lambda}_{both} = \frac{6pz}{\lambda}, \tag{17}$$

then in the stator current spectrum, both RSHs of order λ at previously defined frequencies (13) and (15) appear. These equations show that the position of the RSHs in the stator current spectrum depends on the motor load, i.e., of its slip. This could be a basis for sensor-less speed estimation of a cage rotor induction motor [12], [13].

IV. ROTOR SLOT HARMONICS IN THE STATOR CURRENT SPECTRUM–INVERTER-FED MOTOR

A positive sequence voltage time harmonic of order h, whose frequency is $f_h = hf_m$, produces the magnetomotive force (mmf) waves in the motor air-gap, through the current harmonic it excites. Its distribution over space and time t can be described as follows:

$$F^{a}_{shv}(t, \theta_s) = F^{a}_{shvm} \cos\left(h\omega_m t - vp\theta_s\right). \tag{18}$$

Similarly, the negative sequence voltage time harmonic of order h produces the following mmf wave:

$$F^{b}_{shv}(t, \theta_s) = F^{b}_{shvm} \cos\left(h\omega_m t + vp\theta_s\right). \tag{19}$$

Assuming a uniform air gap width, i.e., by neglecting the slotting effect, the magnetic flux density waves are defined as:

$$B^{a}_{shv}(t, \theta_s) = B^{a}_{shvm} \cos\left(h\omega_m t - vp\theta_s\right), \tag{20}$$
$$B^{b}_{shv}(t, \theta_s) = B^{b}_{shvm} \cos\left(h\omega_m t + vp\theta_s\right). \tag{21}$$

We can now introduce the following transformation of variables,

$$\theta_s = \theta_r + \omega_r t = \theta_r + ((1-s)/p)\,\omega_m t, \tag{22}$$

where θ_r is the position along the air-gap circumference measured in the rotor reference frame. Substituting

$$\begin{aligned} U_{ab}(t) = {} & U_m \cos(\omega_m t - \alpha) + U_{m1}\left(\cos\left(\left(m_f - 2\right)\omega_m t + 2\alpha\right) + \cos\left(\left(m_f + 2\right)\omega_m t + \alpha\right)\right) \\ & + U_{m2}\left(\cos\left(\left(2m_f - 1\right)\omega_m t + \alpha\right) + \cos\left(\left(2m_f + 1\right)\omega_m t - \alpha\right)\right) + U_{m3}\left(\cos\left(\left(3m_f - 2\right)\omega_m t + 2\alpha\right)\right. \\ & \left. + \cos\left(\left(3m_f + 2\right)\omega_m t + \alpha\right)\right) \\ & + U_{m4}\left(\cos\left(\left(3m_f - 4\right)\omega_m t + \alpha\right) + \cos\left(\left(3m_f + 4\right)\omega_m t + 2\alpha\right)\right) + U_{m5}\left(\cos\left(\left(4m_f - 1\right)\omega_m t + \alpha\right)\right. \\ & \left. + \cos\left(\left(4m_f + 1\right)\omega_m t - \alpha\right)\right) \end{aligned} \tag{11}$$

$$\begin{aligned} U_{ab}(t) = {} & U_m \cos(\omega_m t - \alpha) + U_{m1}\left(\cos\left(\left(m_f - 2\right)\omega_m t + 2\alpha\right) + \cos\left(\left(m_f + 2\right)\omega_m t + \alpha\right)\right) \\ & + U_{m2}\left(\cos\left(\left(2m_f - 1\right)\omega_m t + \alpha\right) + \cos\left(\left(2m_f + 1\right)\omega_m t - \alpha\right)\right) + U_{m3}\left(\cos\left(\left(3m_f - 2\right)\omega_m t + 2\alpha\right)\right. \\ & \left. + \cos\left(\left(3m_f + 2\right)\omega_m t + \alpha\right)\right) \\ & + U_{m4}\left(\cos\left(\left(3m_f - 4\right)\omega_m t + \alpha\right) + \cos\left(\left(3m_f + 4\right)\omega_m t + 2\alpha\right)\right) + U_{m5}\left(\cos\left(\left(4m_f - 1\right)\omega_m t - 2\alpha\right)\right. \\ & \left. + \cos\left(\left(4m_f + 1\right)\omega_m t + 2\alpha\right)\right) \end{aligned} \tag{12}$$

(22) into (20) and (21), the magnetic flux density waves viewed from the rotor side are

$$B^a_{shv}(t,\theta_r) = B^a_{shvm}\cos\left(s^a_{hv}\omega_m t - \nu p\theta_r\right), \quad (23)$$

$$B^b_{shv}(t,\theta_r) = B^b_{shvm}\cos\left(s^b_{hv}\omega_m t + \nu p\theta_r\right), \quad (24)$$

where the following slip values are used:

$$s^a_{hv} = h - \nu(1-s), \quad (25)$$

$$s^b_{hv} = h + \nu(1-s). \quad (26)$$

Additionally, in symmetrical three-phase induction motors, fed by a symmetrical system of three-phase voltages, the following spatial harmonic orders exist [14]:

$$\nu = 6k+1, \quad \text{where } k = 0, \pm1, \pm2, \ldots, \quad (27)$$

The corresponding magnetic flux density waves induce electromotive forces (emfs) and thus currents of appropriate frequencies in the short-circuited squirrel-cage rotor winding.

A. RSHS DUE TO DIRECT SEQUENCE PWM TIME HARMONICS

It is common to model the rotor cage as a set of adjacent loops, each embracing two close bars and the end-ring portions connecting them, as explained in [15].

The current in the first rotor loop, arising as a consequence of the magnetic flux density wave (20), produces the following mmf [16],

$$F_{loop1}(t,\theta_r) = \sum_{\mu=1}^{\infty}\frac{2}{\mu\pi}\sin\left(\mu\frac{\pi}{R}\right)I_{r\max}\cos\left(s^a_{hv}\omega_m t\right)\cos(\mu\theta_r) \quad (28)$$

where μ is the spatial harmonic order ($\mu = 1, 2, 3, \ldots$) of rotor loop winding function, assuming that the origin is placed in the center of the first rotor loop, and $I_{r\max}$ is the peak value of the current induced in the loop. The previous expression is decomposed as follows,

$$F_{loop1}(t,\theta_r) = \sum_{\mu=1}^{\infty}K_\mu\left(\cos\left(s^a_{hv}\omega_m t + \mu\theta_r\right) + \cos\left(s^a_{hv}\omega_m t - \mu\theta_r\right)\right) \quad (29)$$

with a suitable definition of the constant K_μ.

In the adjacent rotor loop, displaced by $2\pi/R$ mechanical radians apart from the first, a current of the same intensity and frequency but phase-shifted by $p\cdot\nu\cdot 2\pi/R$ flows. This current produces the following mmf:

$$F_{loop2}(t,\theta_r) = \sum_{\mu=1}^{\infty}K_\mu\left(\begin{array}{l}\cos\left(s^a_{hv}\omega_m t + \mu\theta_r - (\mu+\nu p)\frac{2\pi}{R}\right) + \\ +\cos\left(s^a_{hv}\omega_m t - \mu\theta_r + (\mu-\nu p)\frac{2\pi}{R}\right)\end{array}\right) \quad (30)$$

By summing the mmf of all rotor loops, we obtain:

$$F^a_r(t,\theta_r) = \sum_{i=0}^{R-1}\sum_{\mu=1}^{\infty}K_\mu\left(\begin{array}{l}\cos\left(s^a_{hv}\omega_m t + \mu\theta_r - i\cdot(\mu+\nu p)\frac{2\pi}{R}\right) \\ +\cos\left(s^a_{hv}\omega_m t - \mu\theta_r + i\cdot(\mu-\nu p)\frac{2\pi}{R}\right)\end{array}\right) \quad (31)$$

The previous sum is different from zero in the following cases, [16]:

a) when the condition $\mu = -\nu p$ or $\mu = \nu p$ is satisfied; in such case (31) becomes:

$$F^a_{r1}(t,\theta_r) = F^a_{r1m}\cos\left(s^a_{hv}\omega_m t - \nu p\theta_r\right), \quad (32)$$

b) when condition $\mu + \nu p = \lambda R$ ($\lambda = 1, 2, 3\ldots$) is satisfied; in such case (31) becomes:

$$F^a_{r2}(t,\theta_r) = F^a_{r2m}\cos\left(s^a_{hv}\omega_m t + (\lambda R - \nu p)\theta_r\right), \quad (33)$$

c) when condition $\mu - \nu p = \lambda R$ ($\lambda = 1, 2, 3\ldots$) is satisfied; in such case (31) becomes:

$$F^a_{r3}(t,\theta_r) = F^a_{r3m}\cos\left(s^a_{hv}\omega_m t - (\lambda R + \nu p)\theta_r\right), \quad (34)$$

Based on the variable transformation, (22), these mmf waves, through the assumed uniform air gap, are viewed on the stator side as the following magnetic flux density waves:

$$B^a_{r1}(t,\theta_s) = B^a_{r1m}\cos\left(h\omega_m t - \nu p\theta_s\right), \quad (35)$$

$$B^a_{r2}(t,\theta_s) = B^a_{r2m}\cos\left(\left(h - \lambda\frac{R}{p}(1-s)\right)\omega_m t + \left(\frac{\lambda R}{p} - \nu\right)p\theta_s\right) \quad (36)$$

$$B^a_{r3}(t,\theta_s) = B^a_{r3m}\cos\left(\left(h + \frac{\lambda R}{p}(1-s)\right)\omega_m t - \left(\frac{\lambda R}{p} + \nu\right)p\theta_s\right) \quad (37)$$

Thus, all the magnetic flux density waves resulting from a given time harmonic (of a frequency hf_m) on the stator side are reflected by the rotor back to the stator at the same frequency and two additional, slip-dependent frequencies. The two rotational waves of magnetic flux density given by expressions (36) and (37) can induce emfs in the stator windings and thus excite stator currents with frequencies not present in the voltage source. Of course, this is possible only if the number of pole pairs of the flux density waves (36) and (37) is the same as the number of pole pairs of the magnetic field waves produced by the stator winding itself [17]. By comparing the obtained expressions with the case of a mains-fed induction motor, it is demonstrated that the condition for the existence of RSHs in the stator current spectrum remains unchanged [7], [8]. In contrast, the set of frequencies at which these harmonics occur, changes due to higher-order time harmonics in the supply voltage.

Thus, the lower RSH of order λ exists in the stator current spectrum at the frequency

$$f^{\lambda}_{lower} = \left(h - \lambda\frac{R}{p}(1-s)\right)\cdot f_m, \tag{38}$$

when the following relationship between the number of rotor bars and the number of pole pairs is met,

$$R^{\lambda}_{lower} = \frac{2p\,(3z+1)}{\lambda}, \tag{39}$$

where z is an integer.

The condition for the existence of the upper RSH in the stator current spectrum of the order λ, at the frequency

$$f^{\lambda}_{upper} = \left(h + \lambda\frac{R}{p}(1-s)\right)\cdot f_m, \tag{40}$$

is the following relationship between the number of rotor bars and the number of machine pole pairs:

$$R^{\lambda}_{upper} = \frac{2p\,(3z-1)}{\lambda}. \tag{41}$$

If the number of rotor bars is equal to

$$R^{\lambda}_{both} = \frac{6pz}{\lambda}, \tag{42}$$

then both of the RSHs of order λ with frequencies (38) and (40) appear in the stator current spectrum.

For the most prominent positive sequence higher-order time harmonics in PWM voltage supply, h takes the value $h = 2m_f + 1$. As a consequence, these are the expected frequencies in the stator current spectrum – space harmonics excited by time harmonic of order $2m_f + 1$,

$$f^{\lambda}_{lower2} = \left(2m_f + 1 - \lambda\frac{R}{p}(1-s)\right)f_m \tag{43}$$

$$f^{\lambda}_{upper2} = \left(2m_f + 1 + \lambda\frac{R}{p}(1-s)\right)f_m \tag{44}$$

Obviously, the former of these frequencies may be relatively low. This is especially true when $2m_f$ is close to the ratio between the number of rotor bars and pole pairs - R/p or its multiple. Similar is true also for the time harmonic of order $m_f - 2$, which is prominent for higher values of modulation index m_a, Fig. 4.

B. RSHS DUE TO INVERSE SEQUENCE PWM TIME HARMONICS

Similar analysis can be performed for flux density waves caused by inverse-sequence higher-order time harmonics in the supply voltage. It can be shown that the conditions for the occurrence of RSHs in the stator current spectrum are now inverted compared to the positive sequence.

More precisely, the condition for the existence of the lower RSH of order λ, at frequency (38), is given by expression (41). Similarly, the condition (39) should be met for the presence of the upper RSH of order λ, at frequency (40). If the number of rotor bars is given by the expression (42), then both of RSHs appear in the stator current spectrum.

Now, inverse-sequence time harmonics of the order $2m_f - 1$ and $m_f + 2$, can induce RSHs at rather low frequencies.

V. EXPERIMENTAL SETUP

In order to confirm the analytically obtained results, measurements of the stator current spectrum were performed on a three-phase two-pole squirrel cage induction motor with the following data: 2.2 kW, 400 V, wye connection, 50 Hz, 4.48 A, 2830 rpm. The stator and rotor of the motor have $S = 24$ slots and $R = 18$ bars, respectively. The rotor bars are skewed for one stator slot pitch.

The motor was supplied with a laboratory-built three phase IGBT (Semikron SKM40GD123D) inverter with a DC link voltage of approximately 560 V (diode-rectified three-phase grid voltage). A C2000 Delfino MCU (LaunchXL-F28379D, Texas Instruments) was used for controlling the motor with open-loop control by conventional SVM pulse-width modulation. The launchpad enabled potentiometer-based setting of output and carrier frequencies, and amplitude modulation factors m_a. The motor shaft was coupled to another similar induction motor, operating in generator mode, being supplied by a Danfoss FC-302 frequency converter in an open-loop operating condition.

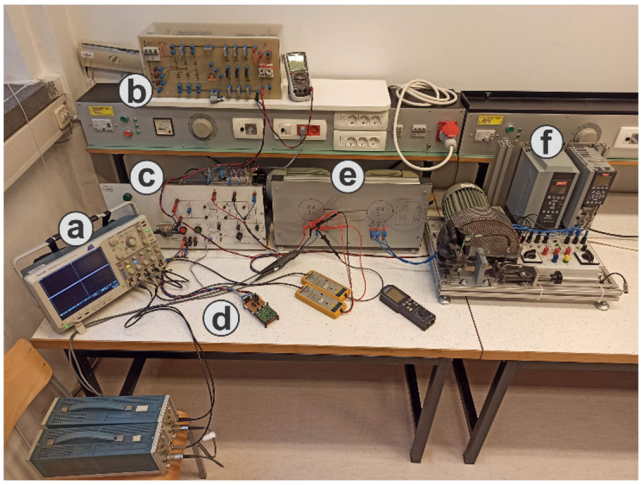

FIGURE 7. Experimental setup, used for stator current measurements of a 2.2 kW induction motor. From left to right are presented Tektronix digital oscilloscope (a), three-phase rectifier (b), three-phase IGBT inverter (c) with MCU launchpad (d), coupled induction motors (e), and a Danfoss frequency converter (f).

Stator current measurements were performed with Tektronix current probes (A6302 with a AM503 amplifier) and a Tektronix DPO4034B 350 MHz oscilloscope. Data were sampled with 1 MS/s for 20 seconds and were stored for post-processing and spectral analysis. The shaft speed was measured with a Chauvin Arnoux C.A 27 tachometer.

VI. RESULTS AND DISCUSSION

A detailed dynamic mathematical model of the selected induction motor was prepared, implementing the winding function theory. It uses the parameterized winding function (PWF) model, in which the number of rotor bars and its skewing angle appear as free parameters [7], [8], [18], [19]. The adoption of such a numerical model, in combination with and independently of experimental results, is deemed to be very effective in order to make the validation complete and

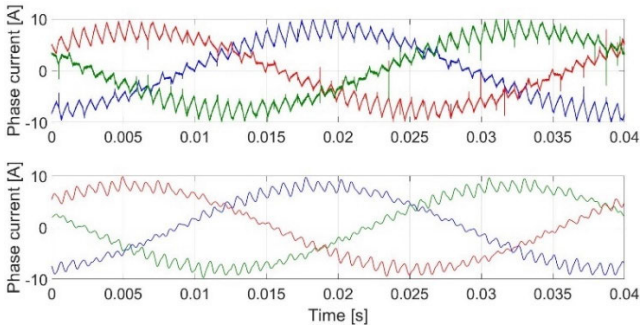

FIGURE 8. Stator phase currents: experimentally recorded (upper plot) and obtained from the mathematical model (lower plot): $f_m = 25$ Hz, $f_c = 625$Hz, $m_a = 0.45$, $m_f = 25$, $U_{dc} = 514$ V.

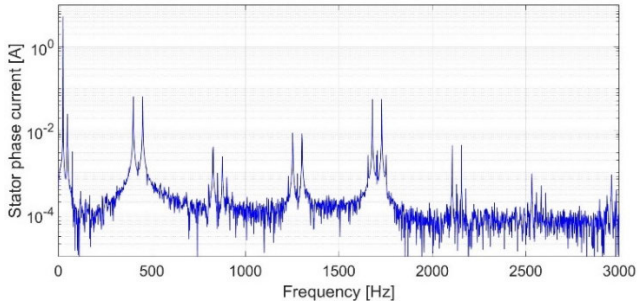

FIGURE 9. Stator phase current spectrum of sinusoidal fed, rated-loaded motor: results from the mathematical model: $f_m = 25$ Hz, $s = 5.29\%$, $U_{ab} = 200$ V.

explanatory, also given the high amount of parasitic effects which may affect measurements.

Just for the sake of illustration, Fig. 8 shows one period of stator phase currents recorded from experiments and obtained from the mathematical model based on the derived analytical expressions (11), (12) for converter voltages.

As a consequence of an unfortunate choice of the number of rotor bars, the motor under test (designed for mains-fed operation) has both of RSHs of each order in the stator current spectrum, at frequencies

$$f^{\lambda}_{lower} = \left(1 - \lambda\frac{R}{p}(1-s)\right)\cdot f_m = (1 - \lambda \cdot 18\,(1-s))\cdot f_m \tag{45}$$

$$f^{\lambda}_{upper} = \left(1 + \lambda\frac{R}{p}(1-s)\right)\cdot f_m = (1 + \lambda \cdot 18\,(1-s))\cdot f_m \tag{46}$$

as the condition (17) is satisfied for $\lambda = 1$ and $z = 3$, $\lambda = 2$ and $z = 6$, $\lambda = 3$ and $z = 9$ etc.

In the case of a mains-fed motor with a frequency of $f_m = 25$ Hz, at its rated load, the stator current spectrum obtained from the simplified mathematical model considering an unskewed rotor is shown in Fig. 9. The first six orders of RSHs are clearly visible. Those of the first order, PSHs, appear at 401.2 Hz and 451.2 Hz. Upper order harmonics appear at frequencies: 827.4 Hz and 877.4 Hz, 1254 Hz and 1304 Hz, 1680 Hz and 1730 Hz etc.

For the rated-loaded, inverter-fed motor, supplied with a fundamental frequency of 25 Hz and a carrier signal

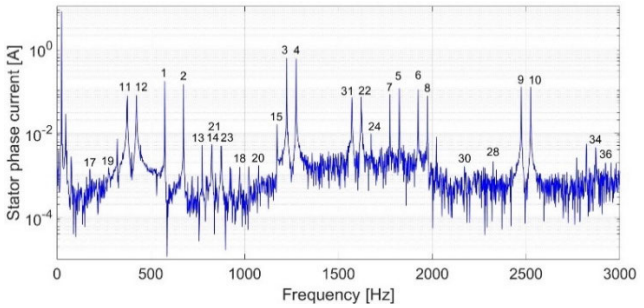

FIGURE 10. Stator phase current spectrum of inverter-fed, rated-loaded motor: results from the mathematical model with unskewed rotor bars: $f_m = 25$ Hz, $f_c = 625$ Hz, $m_a = 0.45$, $m_f = 25$, $s = 11.26\%$.

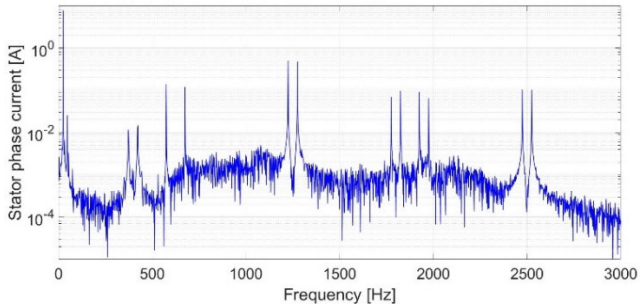

FIGURE 11. Stator phase current spectrum of inverter-fed, rated-loaded motor: results from the mathematical model with rotor bars skewed by one stator slot pitch, $\gamma = 2\pi/S = 2\pi/24$ rad: $f_m = 25$ Hz, $f_c = 625$ Hz, $m_a = 0.45$, $m_f = 25$, $s = 11.63\%$.

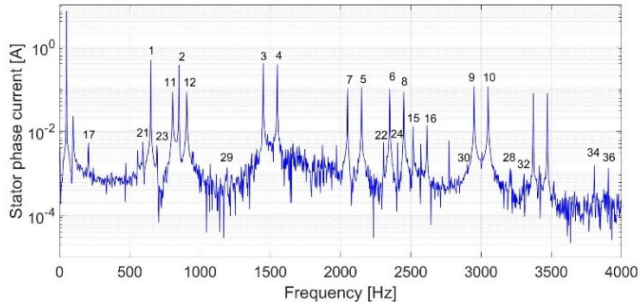

FIGURE 12. Stator phase current spectrum of inverter-fed, rated-loaded motor: results from the mathematical model with unskewed rotor bars: $f_m = 50$ Hz, $f_c = 750$ Hz, $m_a = 0.9$, $m_f = 15$, $s = 4.97\%$.

frequency of 625 Hz and a modulation factor $m_a = 0.45$, with unskewed rotor bars, the stator current spectrum is obtained as shown in Fig. 10. Almost all of the previously predicted components in the stator current spectrum are clearly visible. Their exact frequencies and number designation are given in detail by Table 1 in the Appendix.

In order to observe the effect of skewing of rotor bars by one stator slot pitch, the mathematical model of the motor was modified accordingly [20]. The resulting current spectrum is given in Fig. 11. By comparing this stator current spectrum with the previous one presented in Fig. 10, it is evident that space harmonics are significantly attenuated or even missing for higher orders. This is not the case with time harmonics, instead, as one could expect.

For the case of an inverter-fed motor at rated load, supplied by a fundamental frequency of 50 Hz and a carrier signal frequency of 750 Hz, with a modulation factor $m_a = 0.9$,

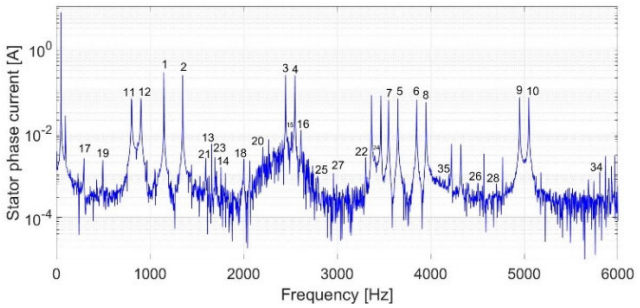

FIGURE 13. Stator phase current spectrum of inverter-fed, rated loaded motor: results from the mathematical model with unskewed rotor bars: $f_m = 50$ Hz, $f_c = 1250$ Hz, $m_a = 0.9$, $m_f = 25$, $s = 5.06\%$.

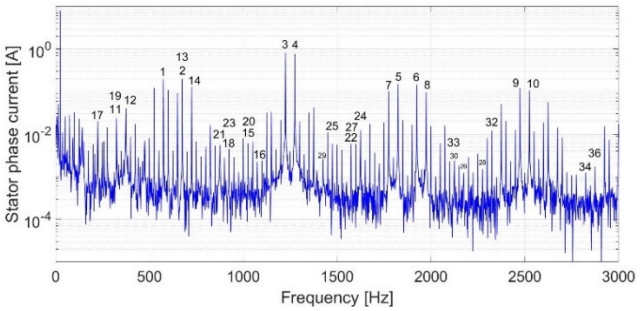

FIGURE 14. Stator phase current spectrum of inverter-fed, rated-loaded motor – from experiment: $f_m = 25$ Hz, $f_c = 625$ Hz, $m_a = 0.45$, $m_f = 25$, $s = 22.33\%$.

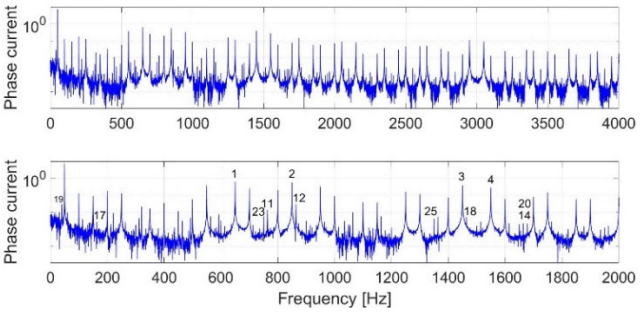

FIGURE 15. Stator phase current spectrum of inverter-fed, rated-loaded motor – from experiment: $f_m = 50$ Hz, $f_c = 750$ Hz, $m_a = 0.9$, $m_f = 15$, $s = 9.72\%$.

the stator current spectrum is obtained from the mathematical model as shown in Fig. 12.

For the same conditions as above, but with a carrier signal frequency of 1250 Hz as well as with a modulation factor $m_a = 0.9$, the stator current spectrum is obtained from the mathematical model, as shown in Fig. 13.

Experimentally recorded stator current spectra for three different modulation frequencies, carrier frequencies, and modulation indexes are given in Figs. 14 – 16. They show a plenty of higher frequency components, predominantly time harmonics due to inverter output. However, the predicted space harmonics exist and are clearly visible, too. All are marked in the figures according to the indexes introduced in Table 1, in the Appendix.

As all of the even number of rotor bars in two-pole cage induction motor produce at least one of the first order RSHs, lower or upper or both of them [8], in order to analyze

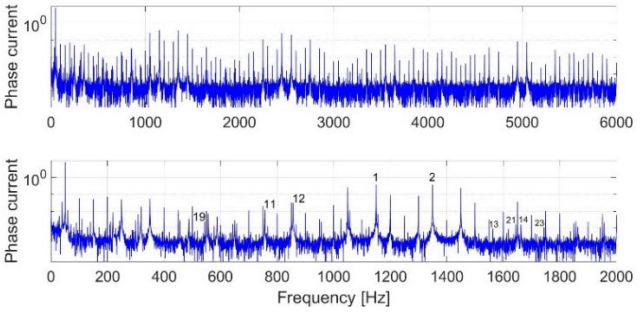

FIGURE 16. Stator phase current spectrum of inverter-fed, rated loaded motor – from experiment: $f_m = 50$ Hz, $f_c = 1250$ Hz, $m_a = 0.9$, $m_f = 25$, $s = 10.38\%$.

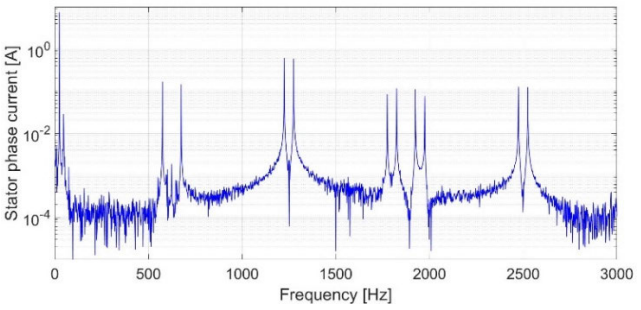

FIGURE 17. Stator phase current spectrum of inverter-fed, rated loaded motor with $R = 27$ rotor bars – results from the mathematical model – rotor bars skewed for one stator slot pitch, $\gamma = 2\pi/S = 2\pi/24$ rad: $f_m = 25$ Hz, $f_c = 625$ Hz, $m_a = 0.45$, $m_f = 25$, $s = 11.28\%$.

the influence of the number of rotor bars on stator current spectrum, an example with an odd number of rotor bars, i.e., $R = 27$, is given in Fig. 17.

According to conditions (39) and (41) neither of the first order RSHs exist in this case. Thus the stator current spectrum contains only time harmonics resulting from the non-sinusoidal inverter output voltage. In addition, the skewing for one stator slot pitch shows similar results as obtained for unskewed rotor – demonstrating only marginal effects [19].

VII. CONCLUSION

The paper initially gives a brief overview of the voltage spectral composition at the output of a carrier-based PWM inverter with min-max sequence injection and presents approximate analytical expressions for line-to-line voltages.

It further shows that the conditions for RSHs in the stator current spectrum of an inverter-fed cage induction motor are identical to the case of mains-fed motors. However, in the former case, each of the time harmonics in line voltages produces its pair of space harmonics, known as RSHs. It is a matter of fact that, as experiments clearly show, the stator current spectrum of an inverter-fed motor includes a multitude of extra harmonics. Some of them directly relate to harmonics present in DC voltage of the inverter whose effect is evident in stator current spectrum when the motor is driven in open-loop control mode. Still, it is undoubtedly desirable not to associate them with harmonics resulting from an unfortunate choice of the number of rotor bars.

TABLE 1. Frequencies of stator phase current higher harmonics: 2.2 kW, 400 V, 50 Hz, 4.48 A, 2830 rpm, $S = 24$, $R = 18$.

		Obtained from the model			Expected in the experimental results		
#	**Time harmonics**	**Figure 10** f_m=25 Hz f_c=625 Hz m_f=25 m_a=0.45 s=0.1126	**Figure 12** f_m=50 Hz f_c=750 Hz m_f=15 m_a=0.9 s=0.0497	**Figure 13** f_m=50 Hz f_c=1250 Hz m_f=25 m_a=0.9 s=0.0506	**Figure 14** f_m=25 Hz f_c=625 Hz m_f=25 m_a=0.45 s=0.2233	**Figure 15** f_m=50 Hz f_c=750 Hz m_f=15 m_a=0.9 s=0.0972	**Figure 16** f_m=50 Hz f_c=1250 Hz m_f=25 m_a=0.9 s=0.1038
1	$(m_f-2)f_m$	575.00 Hz	650.00 Hz	1150.00 Hz	575.00 Hz	650.00 Hz	1150.00 Hz
2	$(m_f+2)f_m$	675.00 Hz	850.00 Hz	1350.00 Hz	675.00 Hz	850.00 Hz	1350.00 Hz
3	$(2m_f-1)f_m$	1225.00 Hz	1450.00 Hz	2450.00 Hz	1225.00 Hz	1450.00 Hz	2450.00 Hz
4	$(2m_f+1)f_m$	1275.00 Hz	1550.00 Hz	2550.00 Hz	1275.00 Hz	1550.00 Hz	2550.00 Hz
5	$(3m_f-2)f_m$	1825.00 Hz	2150.00 Hz	3650.00 Hz	1825.00 Hz	2150.00 Hz	3650.00 Hz
6	$(3m_f+2)f_m$	1925.00 Hz	2350.00 Hz	3850.00 Hz	1925.00 Hz	2350.00 Hz	3850.00 Hz
7	$(3m_f-4)f_m$	1775.00 Hz	2050.00 Hz	3550.00 Hz	1775.00 Hz	2050.00 Hz	3550.00 Hz
8	$(3m_f+4)f_m$	1975.00 Hz	2450.00 Hz	3950.00 Hz	1975.00 Hz	2450.00 Hz	3950.00 Hz
9	$(4m_f-1)f_m$	2475.00 Hz	2950.00 Hz	4950.00 Hz	2475.00 Hz	2950.00 Hz	4950.00 Hz
10	$(4m_f+1)f_m$	2525.00 Hz	3050.00 Hz	5050.00 Hz	2525.00 Hz	3050.00 Hz	5050.00 Hz
	Space harmonics induced by fundamental harmonic	**At frequency**	**At frequency**	**At frequency**	**At frequency**	**At frequency**	**At frequency**
11	$(1-R(1-s)/p)f_m$	374.33 Hz	805.30 Hz	804.44 Hz	324.51 Hz	762.52 Hz	756.58 Hz
12	$(1+R(1-s)/p)f_m$	424.33 Hz	905.30 Hz	904.44 Hz	374.51 Hz	862.52 Hz	856.58 Hz
13	$(1-2R(1-s)/p)f_m$	773.67 Hz	1660.60 Hz	1658.89 Hz	674.03 Hz	1575.04 Hz	1563.16 Hz
14	$(1+2R(1-s)/p)f_m$	823.67 Hz	1760.60 Hz	1758.89 Hz	724.03 Hz	1675.04 Hz	1663.16 Hz
15	$(1-3R(1-s)/p)f_m$	1173.00 Hz	2515.90 Hz	2513.33 Hz	1023.55 Hz	2387.56 Hz	2369.74 Hz
16	$(1+3R(1-s)/p)f_m$	1223.00 Hz	2615.90 Hz	2613.33 Hz	1073.55 Hz	2487.56 Hz	2469.74 Hz
	Space harmonics induced by higher time harmonics	**At frequency**	**At frequency**	**At frequency**	**At frequency**	**At frequency**	**At frequency**
17	$(m_f-2-R(1-s)/p)f_m$	175.67 Hz	205.30 Hz	295.56 Hz	225.49 Hz	162.52 Hz	343.42 Hz
18	$(m_f-2+R(1-s)/p)f_m$	974.33 Hz	1505.30 Hz	2004.44 Hz	924.51 Hz	1462.52 Hz	1956.58 Hz
19	$(m_f+2-R(1-s)/p)f_m$	275.67 Hz	5.30 Hz	495.56 Hz	325.49 Hz	37.48 Hz	543.42 Hz
20	$(m_f+2+R(1-s)/p)f_m$	1074.33 Hz	1705.30 Hz	2204.44 Hz	1024.51 Hz	1662.52 Hz	2156.58 Hz
21	$(2m_f-1-R(1-s)/p)f_m$	825.67 Hz	594.70 Hz	1595.56 Hz	875.49 Hz	637.48 Hz	1643.42 Hz
22	$(2m_f-1+R(1-s)/p)f_m$	1624.33 Hz	2305.30 Hz	3304.44 Hz	1574.51 Hz	2262.52 Hz	3256.58 Hz
23	$(2m_f+1-R(1-s)/p)f_m$	875.67 Hz	694.70 Hz	1695.56 Hz	925.49 Hz	737.48 Hz	1743.42 Hz
24	$(2m_f+1+R(1-s)/p)f_m$	1674.33 Hz	2405.30 Hz	3404.44 Hz	1624.51 Hz	2362.52 Hz	3356.58 Hz
25	$(3m_f-2-R(1-s)/p)f_m$	1425.67 Hz	1294.70 Hz	2795.56 Hz	1475.49 Hz	1337.48 Hz	2843.42 Hz
26	$(3m_f-2+R(1-s)/p)f_m$	2224.33 Hz	3005.30 Hz	4504.44 Hz	2174.51 Hz	2962.52 Hz	4456.58 Hz
27	$(3m_f+2-R(1-s)/p)f_m$	1525.67 Hz	1494.70 Hz	2995.56 Hz	1575.49 Hz	1537.48 Hz	3043.42 Hz
28	$(3m_f+2+R(1-s)/p)f_m$	2324.33 Hz	3205.30 Hz	4704.44 Hz	2274.51 Hz	3162.52 Hz	4656.58 Hz
29	$(3m_f-4-R(1-s)/p)f_m$	1375.67 Hz	1194.70 Hz	2695.56 Hz	1425.49 Hz	1237.48 Hz	2743.42 Hz
30	$(3m_f-4+R(1-s)/p)f_m$	2174.33 Hz	2905.30 Hz	4404.44 Hz	2124.51 Hz	2862.52 Hz	4356.58 Hz
31	$(3m_f+4-R(1-s)/p)f_m$	1575.67 Hz	1594.70 Hz	3095.56 Hz	1625.49 Hz	1637.48 Hz	3143.42 Hz
32	$(3m_f+4+R(1-s)/p)f_m$	2374.33 Hz	3305.30 Hz	4804.44 Hz	2324.51 Hz	3262.52 Hz	4756.58 Hz
33	$(4m_f-1-R(1-s)/p)f_m$	2075.67 Hz	2094.70 Hz	4095.56 Hz	2125.49 Hz	2137.48 Hz	4143.42 Hz
34	$(4m_f-1+R(1-s)/p)f_m$	2874.33 Hz	3805.30 Hz	5804.44 Hz	2824.51 Hz	3762.52 Hz	5756.58 Hz
35	$(4m_f+1-R(1-s)/p)f_m$	2125.67 Hz	2194.70 Hz	4195.56 Hz	2175.49 Hz	2237.48 Hz	4243.42 Hz
36	$(4m_f+1+R(1-s)/p)f_m$	2924.33 Hz	3905.30 Hz	5904.44 Hz	2874.51 Hz	3862.52 Hz	5856.58 Hz

Thus, it can be said that the choice of the appropriate number of rotor bars in the case of an inverter-fed motor is crucial–much more than in the case of mains-fed machines. In the case of three-phase, two-pole motors, this means targeting an adequate number of rotor bars among the odd numbers. Namely, any of the even numbers of rotor bars produces at least one of the PSHs of all orders. In the case of a higher number of pole pairs ($p > 1$), such a number of rotor bars exists even among the even numbers. In fact, according to recently published research, it has been shown that the degree of freedom to choose the appropriate number of rotor bars rises as the number of pole pairs increases.

Additionally, it has been demonstrated that an especially unfavorable case occurs when the frequency modulation ratio, or its multiple, is close to the ratio of the number of rotor bars and pole pairs, or multiple of this ratio. In that case, RSHs in the stator current spectrum can occur at low frequencies, which are therefore more pronounced. The undoubted consequences are increased losses in the motor windings, as well as undesirable noise, vibration, and harshness (NVH) issues.

APPENDIX

See Table 1.

REFERENCES

[1] A. H. VanderMeulen, T. J. Natali, T. J. Dionise, G. Paradiso, and K. Ameele, "Exploring new and conventional starting methods of large medium-voltage induction motors on limited kVA sources," *IEEE Trans. Ind. Appl.*, vol. 55, no. 5, pp. 4474–4482, Sep. 2019.

[2] M. A. Hannan, J. A. Ali, P. J. Ker, A. Mohamed, M. S. H. Lipu, and A. Hussain, "Switching techniques and intelligent controllers for induction motor drive: Issues and recommendations," *IEEE Access*, vol. 6, pp. 47489–47510, 2018.

[3] M. L. De Klerk and A. K. Saha, "A comprehensive review of advanced traction motor control techniques suitable for electric vehicle applications," *IEEE Access*, vol. 9, pp. 125080–125108, 2021.
[4] B. Poudel, E. Amiri, P. Rastgoufard, and B. Mirafzal, "Toward less rare-earth permanent magnet in electric machines: A review," *IEEE Trans. Magn.*, vol. 57, no. 9, pp. 1–19, Sep. 2021.
[5] Y. Wang, L. Tian, L. Zhang, and H. Zhao, "Auto-tracking frequency regulation based energy saving technology for motor systems with dynamic and potential energy load," *IEEE Access*, vol. 9, pp. 131806–131814, 2021.
[6] G. Li, Z. Fu, and Y. Wang, "Electromagnetic vibration and noise suppression of induction motor based on RPWM selective spectrum shaping," *IEEE Access*, vol. 9, pp. 54509–54517, 2021.
[7] G. Joksimovic, M. Mezzarobba, A. Tessarolo, and E. Levi, "Optimal selection of rotor bar number in multiphase cage induction motors," *IEEE Access*, vol. 8, pp. 135558–135568, 2020.
[8] G. Joksimović, E. Levi, A. Kajević, M. Mezzarobba, and A. Tessarolo, "Optimal selection of rotor bar number for minimizing torque and current pulsations due to rotor slot harmonics in three-phase cage induction motors," *IEEE Access*, vol. 8, pp. 228572–228585, 2020.
[9] B. M. Wilamowski and J. D. Irwin, *The Industrial Electronics Handbook, Power Electronics and Motor Drives*, 2nd ed. Boca Raton, FL, USA: CRC Press, 2011.
[10] N. Mohan, T. M. Undeland, and W. P. Robbins, *Power Electronics, Converters, Applications and Design*. Hoboken, NJ, USA: Wiley, 1995.
[11] P. C. Sen, *Principles of Electric Machines and Power Electronics*. Hoboken, NJ, USA: Wiley, 1997.
[12] O. Keysan and H. B. Ertan, "Real-time speed and position estimation using rotor slot harmonics," *IEEE Trans. Ind. Informat.*, vol. 9, no. 2, pp. 899–908, May 2013.
[13] W. L. Silva, A. M. N. Lima, and A. Oliveira, "Speed estimation of an induction motor operating in the nonstationary mode by using rotor slot harmonics," *IEEE Trans. Instrum. Meas.*, vol. 64, no. 4, pp. 984–994, Apr. 2015.
[14] S. N. Vukosavić, *Electrical Machines*. New York, NY, USA: Springer-Verlag, 2012.
[15] T. A. Lipo, *Analysis of Synchronous Machines*. Boca Raton, FL, USA: CRC Press, 2012.
[16] G. Joksimović, M. Đurović, and J. Penman, "Cage rotor MMF: Winding function approach," *IEEE Power Eng. Rev.*, vol. 21, no. 4, pp. 64–66, Apr. 2001.
[17] G. M. Joksimović, J. Riger, T. M. Wolbank, N. Perić, and M. Vašak, "Stator-current spectrum signature of healthy cage rotor induction machines," *IEEE Trans. Ind. Electron.*, vol. 60, no. 9, pp. 4025–4033, Sep. 2013.
[18] G. Joksimović, "Dynamic model of cage induction motor with number of rotor bars as parameter," *J. Eng.*, vol. 2017, no. 6, pp. 205–211, Jun. 2017.
[19] G. Joksimović, J. I. Melecio, P. M. Tuohy, and S. Djurović, "Towards the optimal 'slot combination' for steady-state torque ripple minimization: An eight-pole cage rotor induction motor case study," *Electr. Eng.*, vol. 102, no. 1, pp. 293–308, Mar. 2020.
[20] J. M. Gojko, D. D. Momir, and O. B. Aleksandar, "Skew and linear rise of MMF across slot modelling-winding function approach," *IEEE Trans. Energy Convers.*, vol. 14, no. 3, pp. 315–320, Sep. 1999.

GOJKO JOKSIMOVIĆ (Senior Member, IEEE) received the M.Sc. and Ph.D. degrees in electrical power engineering from the University of Montenegro, Podgorica, Montenegro, in 1995 and 2000, respectively. Since May 2011, he has been a Full Professor with the University of Montenegro. He has authored some books, one international scientific monograph, and a number of articles published in leading international scientific journals. His main research interests include mathematical modelling and analysis of electrical machines from condition monitoring and design optimization point of view. He was a recipient of the Alexander von Humboldt Research Fellowship.

PETER ZAJEC (Member, IEEE) received the M.Sc. and Ph.D. degrees in electrical engineering from the University of Ljubljana, Ljubljana, Slovenia, in 1997 and 1999, respectively. He is currently an Associate Professor with the Faculty of Electrical Engineering, University of Ljubljana. His main research interests include multi-cell power converters, components optimization, and measuring transducer in power electronics.

ALBERTO TESSAROLO (Senior Member, IEEE) received the Laurea degree in electrical engineering from the University of Padova, in 2000, and the Ph.D. degree in electrical engineering from the University of Trieste, Italy, in 2011. Before joining the University, he was involved in the design and development of large innovative motors, generators, and drives. Since 2006, he has been with the Engineering and Architecture Department, University of Trieste, where he currently teaches the courses in electric machine fundamentals and electric machine design as a Full Professor. He has authored over 180 international articles in the areas of electrical machines and drives. He is a member of the Rotating Machinery Technical Committee TC2 (rotating electric machinery) of the International Electrotechnical Commission (IEC). He is the Editor-in-Chief of the IEEE TRANSACTIONS ON ENERGY CONVERSION.

VANJA AMBROŽIČ (Senior Member, IEEE) received the B.S., M.S., and Ph.D. degrees from the Faculty of Electrical Engineering, University of Ljubljana, Slovenia, in 1986, 1990, and 1993, respectively. In 1986, he joined the Laboratory of Control Engineering, Faculty of Electrical Engineering, University of Ljubljana, first as a Junior Researcher and then an Assistant Professor and an Associate Professor, and is currently a Full Professor with the Department of Mechatronics. His main research interests include the control of electrical drives and power electronics. He is also the Editor-at-Large of *IET Power Electronics*, an Associate Editor of *IET Electric Power Applications*, and a former Associate Editor of *IEEE Industrial Electronics*.

ANDRAŽ RIHAR (Member, IEEE) received the M.Sc. and Ph.D. degrees in electrical engineering from the University of Ljubljana, Ljubljana, Slovenia, in 2012 and 2016, respectively. He is currently a Teaching Assistant with the Faculty of Electrical Engineering, University of Ljubljana. His main research interests include multi-phase and multi-level power converters, data analysis, and processing algorithms.